Guidelines for band gap opening in graphene superlattices with periodic π-vacancy distribution

Diyan Unmu Dzujah,[1] Hongde Yu,[1] and Thomas Heine[1,2,3,*]

[1]*Faculty of Chemistry and Food Chemistry, Technische Universität Dresden, 01062 Dresden, Germany*

[2]*Center for Advanced System Understanding CASUS, Helmholtz-Zentrum Dresden-Rossendorf e. V., 01328 Dresden, Germany*

[3]*Department of Chemistry, Yonsei University, Seodaemun-gu, Seoul 03722, Republic of Korea*

(Received 25 March 2026; revised 16 July 2026; accepted 1 October 2026; published 4 November 2026)

Periodic π-vacancies in graphene superlattices (GSLs) provide a symmetry-based route to band gap opening in graphene by modifying the π-band dispersion, yet the symmetry conditions that determine whether a vacancy motif can open a band gap remain unclear. Here, we investigate periodic π-vacancy GSLs using a nearest-neighbor tight-binding model with one p_z orbital per carbon site to identify the symmetry requirements for band gap opening. Here, π vacancies, resembling functionalized, substituted, or missing carbon sites, are modeled as site deletions in the π basis, and the corresponding hopping matrix elements to and from the deleted sites are set to zero. We focus on π-vacancy motifs with C_2 and C_3 point groups. A $3n \times 3n$ GSL, where $n = 1, 2, 3, \ldots$ is the integer scaling factor multiplying the honeycomb primitive-cell vectors, is required to fold K and K' to Γ, which is one of the requirements for opening a band gap. For C_3-type vacancies, the Dirac cones are pinned at the high-symmetry points, thus remaining at Γ in the folded $3n$ GSLs. However, those C_2-type vacancies, which reduce the global point group of the GSL to D_{2h} by preserving a pair of perpendicular mirror symmetries ($\sigma_v \perp \sigma_d$), can constrain the positions of Dirac cones at Γ. The absence of the σ_v and σ_d planes allows the cones to shift around Γ ($\pm\Delta\mathbf{q}$, $\pm\Delta\mathbf{q}$) in the $3n$ superlattice. The C_3-type vacancies open a relatively larger band gap than the C_2-type vacancies due to twofold degeneracy at Γ, while the C_2-type vacancies leave the GSL with nondegenerate bands. The energy contours near the Dirac cone for C_3-symmetric vacancies remain isotropic, while the absence of C_3 generates anisotropic cones. The band gap openings in $3n$ superlattices scale linearly with defect concentration for each vacancy motif, with the D_{6h} motif yielding the largest gap, reaching 314 meV at only 3.7% defect concentration. Disorder of the superlattice by missing vacancies or by vacancy displacements of one or two primitive lattice vectors of graphene breaks the C_3 symmetry, lifts the degeneracy, and reduces the gap toward the pristine graphene limit.

DOI: 10.1103/nbm9-xhj9

I. INTRODUCTION

Graphene exhibits symmetry-protected Dirac cones at K and K' and is intrinsically gapless in the absence of spin-orbit coupling [1]. Dirac cones yield linear band dispersion near the inequivalent K and K' valleys, allowing electrons to behave as Dirac quasiparticles with Fermi velocity $v_F \approx 10^6$ m/s, giving rise to high carrier mobility and unusual transport properties [2–4]. Despite these electronic properties, the absence of a band gap in monolayer graphene limits its application in electronic devices that require one, such as field-effect transistors. This limitation has motivated extensive work on band gap engineering in graphene, including chemical doping [5–7], vacancies [8–10], functionalization [11–13], and Kekulé-type bond modulation [14]. Among these approaches, periodic π-vacancies are a particularly effective approach to defect engineering because they directly modify the π-electron network and disrupt the bipartite hopping connectivity. Within the tight-binding (TB) framework, the relevant defects are often π-vacancy patterns involving several neighboring sites rather than single-site vacancies [9,10]. The π vacancies are removed sites in the TB Hamiltonian which reflect local functionalization, e.g., by BN substitution [5–7] or by forming additional bonds leading to transformation into sp^3 sites [12,13,15]. From this perspective, a π-orbital TB description offers a direct framework that captures the essential physics of gap opening while remaining computationally efficient for large GSLs.

Graphene defects can be introduced experimentally either in an aperiodic or periodic manner. Aperiodic defects can be introduced through top-down processes, such as electron/ion irradiation, which create vacancies by knocking out carbon atoms [16,17], or plasma etching [18,19]. These methods are valued for their scalability up to the wafer scale; however, the lack of atomic precision and uncontrolled defect geometry can affect the reproducibility of band gap opening [16,17,19]. In contrast, bottom-up approaches can yield well-ordered periodic defect arrays through molecular assembly, providing near-atomic-level precision in defect placement [20–22]. In defected graphene, the band gap depends on the shape, size, and arrangement of the defect patterns [18]. However, realistic structures still exhibit motif displacement [19,20,23,24], which alters the effective symmetry of the perturbation and

*Contact author: thomas.heine@tu-dresden.de

Published by the American Physical Society under the terms of the Creative Commons Attribution 4.0 International license. Further distribution of this work must maintain attribution to the author(s) and the published article's title, journal citation, and DOI.

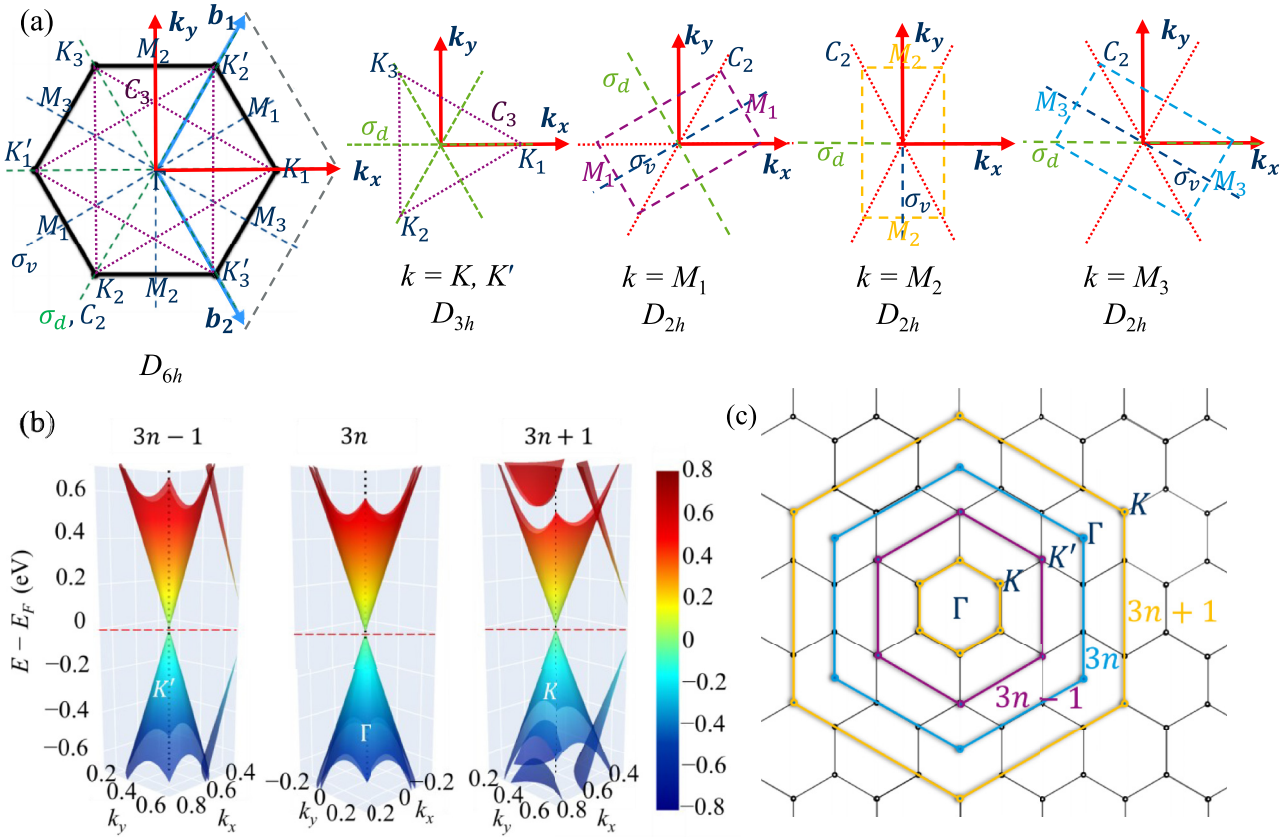


FIG. 1. (a) Graphene BZ showing reciprocal lattice vectors $\mathbf{b}_1$ and $\mathbf{b}_2$, the global point group D_{6h}, and the little group at each high-symmetry point (Γ, K, K', M_1, M_2, and M_3). Representative mirror symmetries across Γ-M $\sigma_v : (k_x, k_y) \to (-k_x, k_y)$ and Γ-K $\sigma_d : (k_x, k_y) \to (k_x, -k_y)$ are repeated every 120°, resulting in three mirror lines for each of σ_v and σ_d. The C_2 and three σ_v planes interchange K and K', while the three σ_d planes connect $K_1 \to K_1$ and $K_2 \leftrightarrow K_3$. Combining C_3 with three σ_d or σ_v planes gives the little group D_{3h} at K and K'. The M_1, M_2, and M_3 points are the midpoints of the BZ edges and have the little group D_{2h}. (b) Dirac point locations for all supercell sizes of pristine graphene. (c) Schematic band folding mechanism in pristine graphene, illustrating how valleys are mapped into the reduced zone.

thereby modifies the electronic properties, including band gap suppression.

Introducing a periodic pattern of vacancies creates a periodic superlattice modulation in the system [25,26]. A superlattice is defined by a real-space periodicity larger than a primitive cell of graphene, thereby reducing the Brillouin zone (BZ) to a mini-BZ (mBZ) and backfolding the pristine bands. Previously studied examples include graphene antidot lattices, also known as nanomesh graphene, and related periodic porous carbon networks that modulate the periodic potential in graphene superlattices (GSLs) [9,27,28]. Authors of prior work have shown that the band dispersions of GSLs are symmetry dependent [10,29,30], and identifying the relevant symmetries provides a practical route to gap opening in GSLs. In the TB model, the Dirac cone in pristine graphene is protected by time-reversal and inversion symmetries, which map K and K', together with sublattice symmetry, which enforces a symmetric spectrum [31], with the global point group of graphene being D_{6h}. The cones at K_1, K_2, and K_3 in the BZ of pristine graphene are related by a C_3 rotation, as are K_1', K_2', and K_3', and C_2 swaps K and K', as shown in Fig. 1(a). Authors of theoretical studies of graphene antidot lattices using TB have predicted that a band gap can be opened in the $3n \times 3n$ superlattice, yielding a fourfold degeneracy at the Γ point [32–34]. This is a direct consequence of the translational symmetry $\mathrm{T_R} : \mathbf{r} \to \mathbf{r} + \mathbf{R}$ in graphene, which determines the folding positions of the Dirac cones across different supercell sizes, interchanges the folded locations of K and K' between the $3n + 1$ and $3n - 1$ supercells, and pins both K and K' at Γ in the $3n$ supercells, as shown in Figs. 1(b) and 1(c). Therefore, the symmetry constraints acting in the folded low-energy subspace can be used to formulate design rules for vacancy superlattices.

To make this explicit, within the π-orbital TB model, graphene is described as a bipartite lattice with sublattices A and B, where the Bloch Hamiltonian can be written as

$$H(\mathbf{k}) = \begin{bmatrix} \varepsilon_{pz} & f(\mathbf{k}) \\ f^*(\mathbf{k}) & \varepsilon_{pz} \end{bmatrix}, \tag{1}$$

where $\varepsilon_{pz} = 0$ and $f(\mathbf{k})$ is the structure factor encoding the nearest-neighbor hoppings, $f(\mathbf{k}) = -t \sum_{n=1}^{3} e^{i\mathbf{k}\cdot\delta_n}$, t is the nearest-neighbor hopping amplitude, and δ_n are the nearest-neighbor vectors connecting A and B sites, and the dispersion energy is then $E_\pm(\mathbf{k}) = \pm|f(\mathbf{k})|$. The Dirac points arise when the sum of the Fourier components vanishes, which occurs at K and K', where $f(K) = f(K') = 0$. A first-order Taylor expansion about K, with $\mathbf{k} = \mathbf{K} + \mathbf{q}$ and $|\mathbf{q}| \ll |\mathbf{K}|$, yields a dispersion linear in $|\mathbf{q}|$ [2]. The formulation shows that

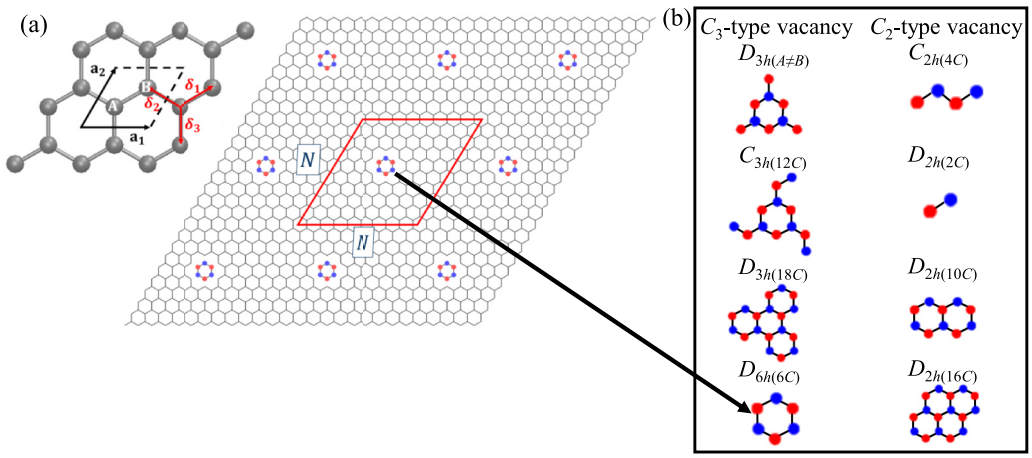


FIG. 2. (a) $N \times N$ GSL defined by the integer scaling factor n applied to the primitive lattice vectors $\mathbf{a}_1$ and $\mathbf{a}_2$. Red (blue) markers denote removed sites on the a (b) sublattices used to model the π vacancies. (b) C_2- and C_3-type π vacancies considered in this work.

periodic modification of the π network in graphene can be viewed as a modulation of the structure factor, which controls the low-energy dispersion of the GSL.

Authors of previous studies have predominantly focused on highly symmetric defect motifs and superlattices [9,10,27,30], whereas lower-symmetry configurations, which may arise from structural imperfections or experimental disorder, have received comparatively less attention. In this work, we establish symmetry-based guidelines for band gap opening in periodic π-vacancy GSLs using a TB framework that captures the low-energy physics associated with the missing π states. We determine how point-group constraints govern symmetry-allowed gap formation and how these constraints depend on the $3n$ superlattice commensurability condition, which is a prerequisite for band gap opening. Additionally, we investigate how vacancy displacement modifies the effective symmetry of the superlattice. We then assess how this symmetry reduction impacts the robustness and magnitude of the band gap. We find that robust and substantial gap opening in $3n$ superlattices occurs when C_3 symmetry is preserved. In contrast, a smaller band gap is obtained when the sufficient symmetry condition of two orthogonal mirror planes remains satisfied. Otherwise, gap opening is not guaranteed. Finally, we show how motif displacement lowers the effective symmetry and suppresses the gap by lifting the twofold degeneracies.

II. METHODS

The GSLs with periodic vacancies are modeled using the TB method implemented in the PythTB package [35]. In this study, we neglect spin polarization and spin-orbit coupling, so the dispersion is spin independent and time-reversal symmetry is preserved. The band structures of the GSLs are treated within the nearest-neighbor approximation, with $t = -2.7$ eV and the on-site energy $\varepsilon_i = 0$. The TB Hamiltonian is defined as

$$H = \sum_i \varepsilon_i c_i^\dagger c_i + \sum_{\langle i,j \rangle} t\, c_i^\dagger c_j, \tag{2}$$

where $c_i^\dagger$ is the creation operator, c_j is the annihilation operator for the p_z orbital on site i, and $\langle i, j \rangle$ denotes the nearest-neighbor pairs. The vacancy periodicity is set by an $N \times N$ superlattice, where $N = 3n-1$, $3n$, or $3n+1$, and $n = 1, 2, 3, \ldots$ is the integer scaling factor of the honeycomb primitive-cell vectors $\mathbf{a}_1$ and $\mathbf{a}_2$, as shown in Fig. 2(a), and the graphene lattice constant is defined as $a = |\mathbf{a}_1| = |\mathbf{a}_2|$. The vacancies are modeled by removing the p_z orbital of C atoms in the GSL. We focus on C_3-type vacancies ($C_{3h(12C)}$, $D_{3h(A\neq B)}$, $D_{3h(18C)}$, and $D_{6h(6C)}$) and C_2-type vacancies ($C_{2h(4C)}$, $D_{2h(2C)}$, $D_{2h(10C)}$, and $D_{2h(16C)}$) as shown in Fig. 2(b).

III. RESULTS AND DISCUSSIONS

Different π-vacancy types in the GSL induce different effects in the band structure. In general, we observe three effects upon introducing a periodic vacancy to the GSL, namely, (i) zero modes, where the eigenvalues remain at zero energy across momentum space and appear as a flat band; (ii) the shift of the Dirac cones toward low-symmetry points in the BZ; and (iii) band gap opening. Vacancies with $A \neq B$ generate at least m zero-energy modes, where $m = |A - B|$, due to the sublattice imbalance, consistent with Lieb's theorem [36]. For example, D_{3h} vacancy shows flat bands, as shown in Table I in the Supplemental Material [37], and may induce magnetic properties [29,36,38,39]. Therefore, in this study, we focus on cases with $A = B$, which is required for band gap opening in the GSL. The effects (ii) and (iii) are discussed in the following sections.

A. Position of the Dirac cone

The position of the Dirac cones in momentum space is dictated by the symmetry of the structure. Here, C_3 symmetry enforces that the two valleys K and K' are 120° rotationally equivalent. Loss of C_3 symmetry in the GSL can shift the position of the Dirac cone in reciprocal space by $\Delta\mathbf{q}$ or, if certain symmetry requirements are met, may lead to band gap opening. It is important to note that the Dirac points can shift to low-symmetry points that lie off the high-symmetry pathways and therefore do not appear in common band

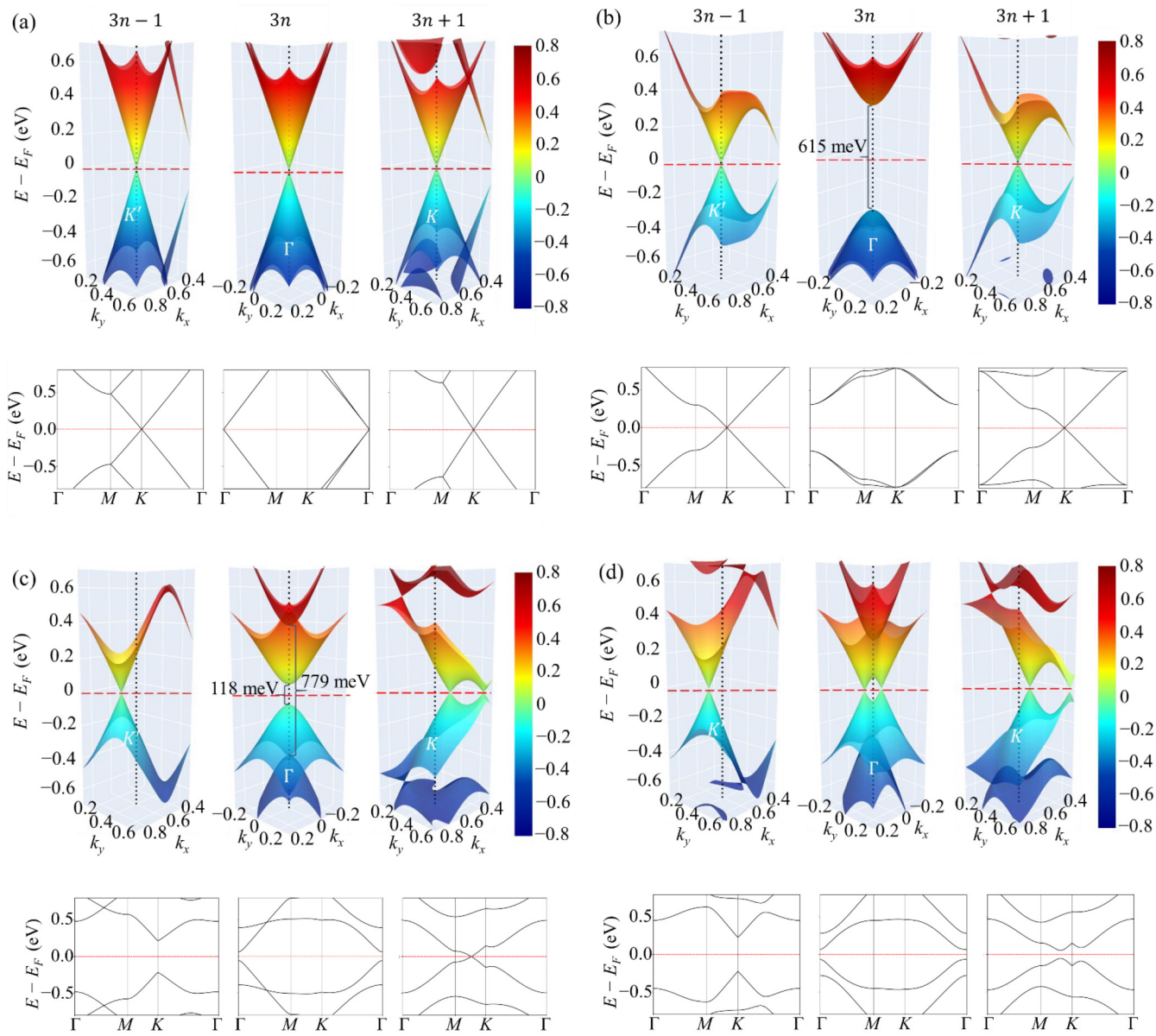


FIG. 3. 2D (top) and one-dimensional (1D; bottom) band structure of (a) pristine graphene, GSLs with (b) $D_{3h(18C)}$, (c) $D_{2h(16C)}$, and (d) $C_{2h(4C)}$ vacancies for superlattice sizes $3n-1$, $3n$, and $3n+1$, where $n=3$, E_F is denoted by the red dash. The band structures of other vacancy motifs can be found in Table I in the Supplemental Material [37].

structure plots. Therefore, plotting the two-dimensional (2D) band structure is essential to visually observe the effect of this perturbation, as shown in Fig. S1 in the Supplemental Material [37]. The 2D band structures of pristine graphene are depicted in Fig. 3(a), showing that Dirac cones are located at the high-symmetry points in each superlattice. The introduction of the C_3-type vacancy in the GSL keeps the Dirac cones at high-symmetry points, as shown in Fig. 3(b); thus, any band gap opening can be observed by sampling these points. In contrast, the absence of the C_3 axis can shift the Dirac cones to $K \pm \Delta\mathbf{q}$ in the $3n-1$ and $3n+1$ superlattices, as depicted in Figs. 3(c) and 3(d). The magnitude of $\Delta\mathbf{q} \propto$ defect concentration, meaning a small perturbation of the C_2-type vacancy leads to minimal $\Delta\mathbf{q}$.

B. Band gap opening in the GSL and the effect of C_3 and $\sigma_d \perp \sigma_v$

A necessary condition for the band gap opening in a GSL is that both K and K' are folded onto the time-reversal invariant momenta (TRIM) point Γ [33], which occurs when the superlattice size is $3n$. The C_3-type vacancy in the GSL makes the folding straightforward due to the absence of $\Delta\mathbf{q}$, keeping the Dirac cone at a high-symmetry point. Figure 3(b) shows the positions of the Dirac cones in $3n-1$, $3n$, and $3n+1$ for $n=3$ with a $D_{3h(18C)}$ vacancy. A band gap of $|\Delta_g| = 615$ meV is observed at Γ in the $3n$ superlattice. The previously observed fourfold degeneracy at E_F is split into a twofold degeneracy, with the global point group of the mBZ being D_{3h}. The little group is D_{3h} at K and K' and D_{2h} at the M points. In the GSL containing $D_{3h(18C)}$ vacancy, the

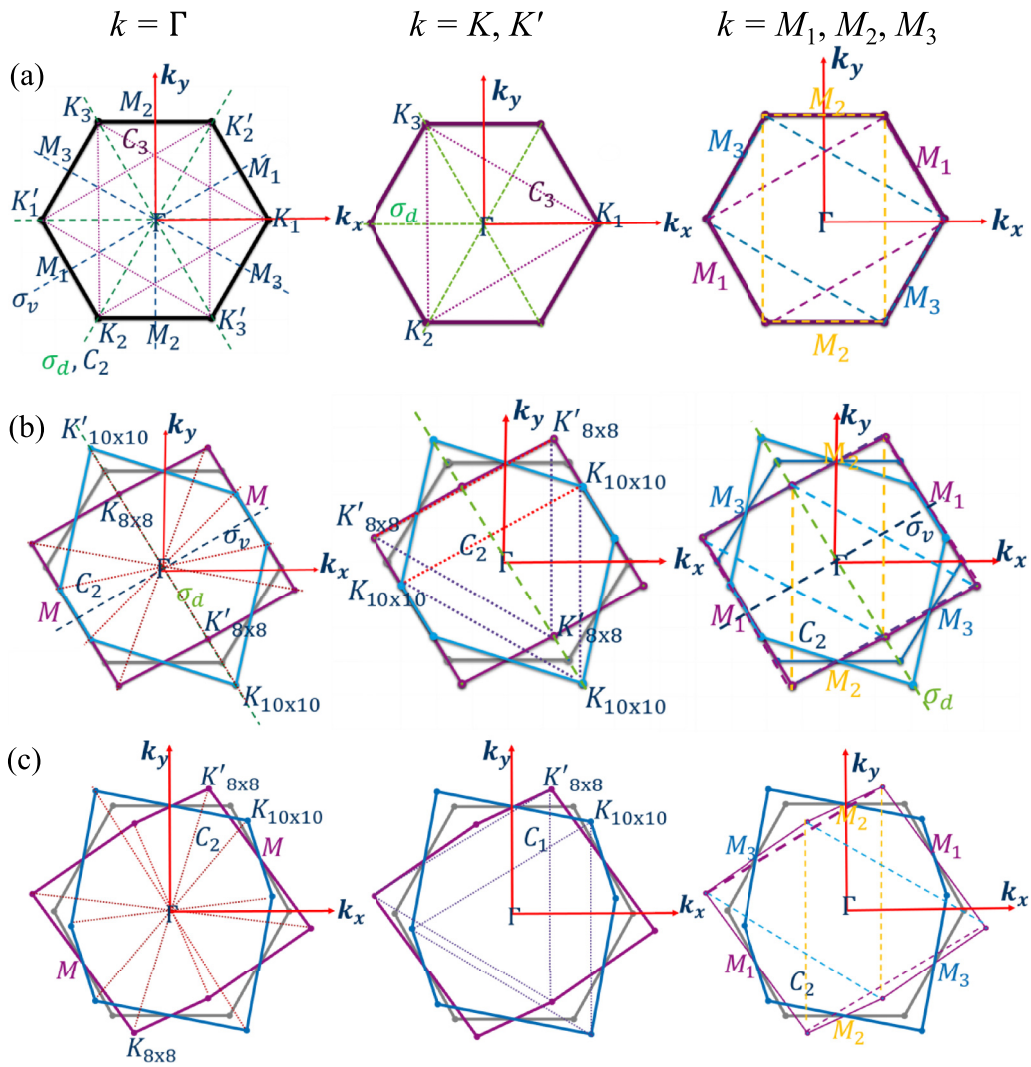


FIG. 4. Reduced little groups at the high-symmetry points (Γ, K, K', M_1, M_2, and M_3) in the GSL with (a) $D_{3h(18C)}$, (b) $D_{2h(16C)}$, and (c) $C_{2(4C)}$ vacancies for superlattice sizes 8×8 and 10×10.

identity, time-reversal, inversion, C_2, C_3, $3\sigma_v, 3\sigma_d$, and σ_h symmetries are well preserved, as illustrated in Fig. 4(a). The periodic vacancy in GSL with sublattice removal $A = B$ keeps the sublattice symmetry and preserve the bipartite form of the Hamiltonian matrix. This shows that the matrix chirality $\Gamma H \Gamma^{-1} = -H$, $\Gamma^2 = I$ is preserved, leading to symmetric eigenvalues around E_F in all GSL sizes. The $E(k) = -E(k)$ at the conduction band minimum (CBM) and valence band maximum (VBM) in the $3n$ GSL can be seen in Fig. 3. As a result, a band gap opens.

In contrast, whether C_2-type vacancies without a C_3 rotational axis open a band gap depends on which symmetries remain in the mBZ and whether the superlattice periodicity permits momentum space commensurability. Figures 3(b) and 4(b) show the positions of the Dirac cones in the GSL with a $D_{2h(16C)}$ vacancy slightly shifted off the high-symmetry point due to the breaking of C_3 symmetry, leading to a reduction of the little group at K and K' to $C_{2v} = (E, C_2, \sigma_d, \sigma_h)$, with the little group at M_1 remaining D_{2h}, while M_2 and M_3 are reduced to C_{2h}. A direct consequence of C_3 breaking is the loss of at least two σ_d and two σ_v mirror planes because the product of $\sigma^{0^\circ}\sigma^{60^\circ} = C_{120^\circ} = C_3$, which is not possible after losing the C_3 axis, reducing the point group of the mBZ to D_{2h}. In this case, despite $\Delta\mathbf{q} \neq 0$ in the $3n-1$ and $3n+1$ GSLs, in the $3n$ GSLs, both K and K' can still fold to Γ and open a band gap of 118 meV, as seen in Fig. 3(c). The $D_{2h(16C)}$ GSL preserves one pair of $\sigma_d \perp \sigma_v$ mirror planes, with one σ_d constraining K and K' to shift only along the mirror line $k_{||}$, while shifts perpendicular to the mirror line $k_\perp$ are forbidden, reducing the global point group to D_{2h}, as shown in Fig. 4(b). Additionally, the constraints imposed by the $\sigma_d \perp \sigma_v$ planes lock K and K' at $k = \Gamma = (0, 0)$ in the $3n$ GSL because both mirrors forbid the shift along $k_\perp$ perpendicular to each other. Among the C_2-type vacancies studied in this work, the $D_{2h(2C)}$, $D_{2h(10C)}$, and $D_{2h(16C)}$ vacancies preserve one pair of $\sigma_d \perp \sigma_v$ planes, as shown in Fig. 4(b) and Fig. S2 in the Supplemental Material [37]. These C_2-type vacancies preserve identity, time-reversal, inversion, C_2, σ_v, σ_d, and σ_h symmetries. The $C_{2h(4C)}$ vacancy breaks all three σ_v and σ_d mirror planes in the mBZ, leaving no constraint to pin K and K' during band folding to Γ in the $3n$ GSL, allowing the shift $(\pm\Delta\mathbf{q}, \pm\Delta\mathbf{q})$ around Γ, preventing the folding of K and K'

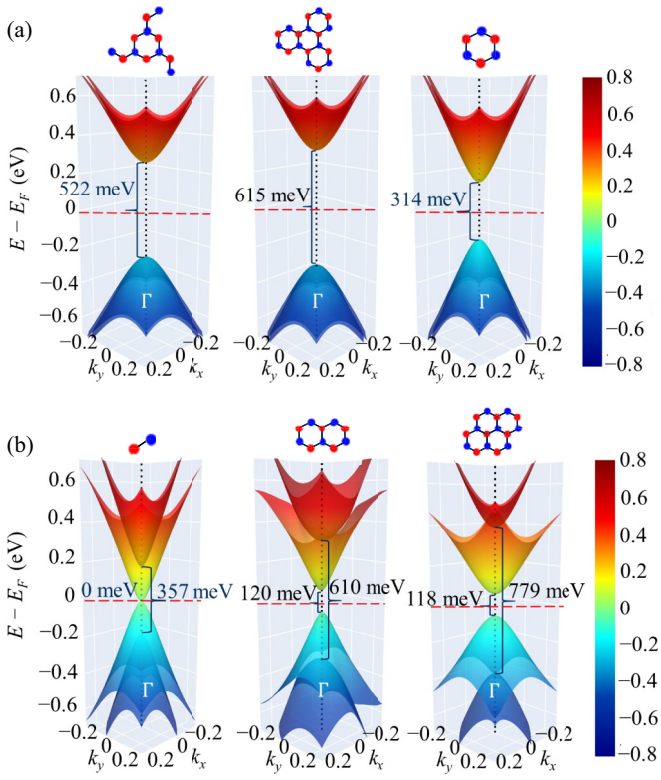


FIG. 5. Band structures $3n$ GSLs with (a) C_3-type vacancies and (b) C_2-type vacancies, with $n = 3$, illustrating the influence of symmetry on band gap opening around Γ.

to Γ in the $3n$ GSL and reducing the point group of the mBZ and the little groups at M_1, M_2, and M_3 to C_{2h}, while the little groups at K and K' are C_s, as shown in the Fig. 4(c). These types of GSLs preserve identity, time-reversal, inversion, C_2, and σ_h symmetries and keep the GSL gapless, as shown in Fig. 3(d). Thus, the sufficient symmetries in the mBZ for C_2-type vacancies to enforce the locking of K and K' to Γ in $3n$ GSLs are a pair of perpendicular mirror planes $\sigma_d \perp \sigma_v$.

Band gaps obtained from the C_2-type vacancies are smaller than those from the C_3-type vacancies. This is a consequence of breaking the doubly degenerate states at $\pm\frac{1}{2}|\Delta E_1|$ into nondegenerate states near E_F as shown in Figs. 5 and 6, indicating the loss of C_3 symmetry in the GSL. A higher defect concentration or a smaller superlattice size leads to a larger band gap in the GSL. Here, the defect concentration is defined as the percentage of removed π orbitals relative to the total number of π orbitals in the pristine graphene $N \times N$ supercell. With decreasing perturbation, the characteristics of the GSL become closer to those of pristine graphene; this is depicted in Figs. 6(a) and 6(b). Figure 6(b) shows that the band gap opening in $3n$ superlattices follows a linear trend for each vacancy motif, as summarized in Table III in the Supplemental Material [37], with $D_{6h(6C)}$ yielding the widest band gap as a function of defect concentration, reaching 314 meV at a defect concentration of only 3.70%. By comparison, $C_{3h(12C)}$ and $D_{3h(18C)}$ require defect concentrations of 4.17% and 6.25% to reach 295 and 345 meV, respectively. In contrast, smaller band gaps are obtained for C_2-type vacancies. Here, $D_{2h(10C)}$ requires a defect concentration of 6.17% to reach 120 meV, whereas $D_{2h(16C)}$ requires 9.88% to reach

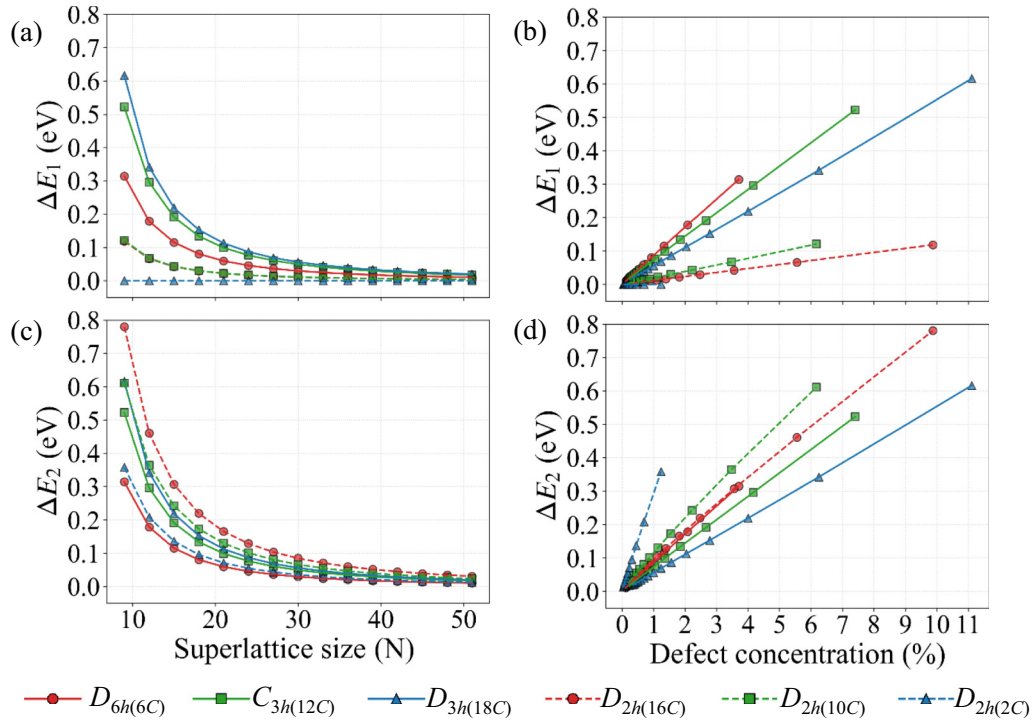


FIG. 6. Band gap ΔE_1 as a function of (a) superlattice size N and (b) defect concentration. Band-splitting energy ΔE_2 for C_2-type vacancies and the degenerate band energy for C_3-type vacancies as functions of (c) superlattice size N and (d) defect concentration. All plots correspond to $3n$ GSLs with $n = 3, \ldots, 17$.

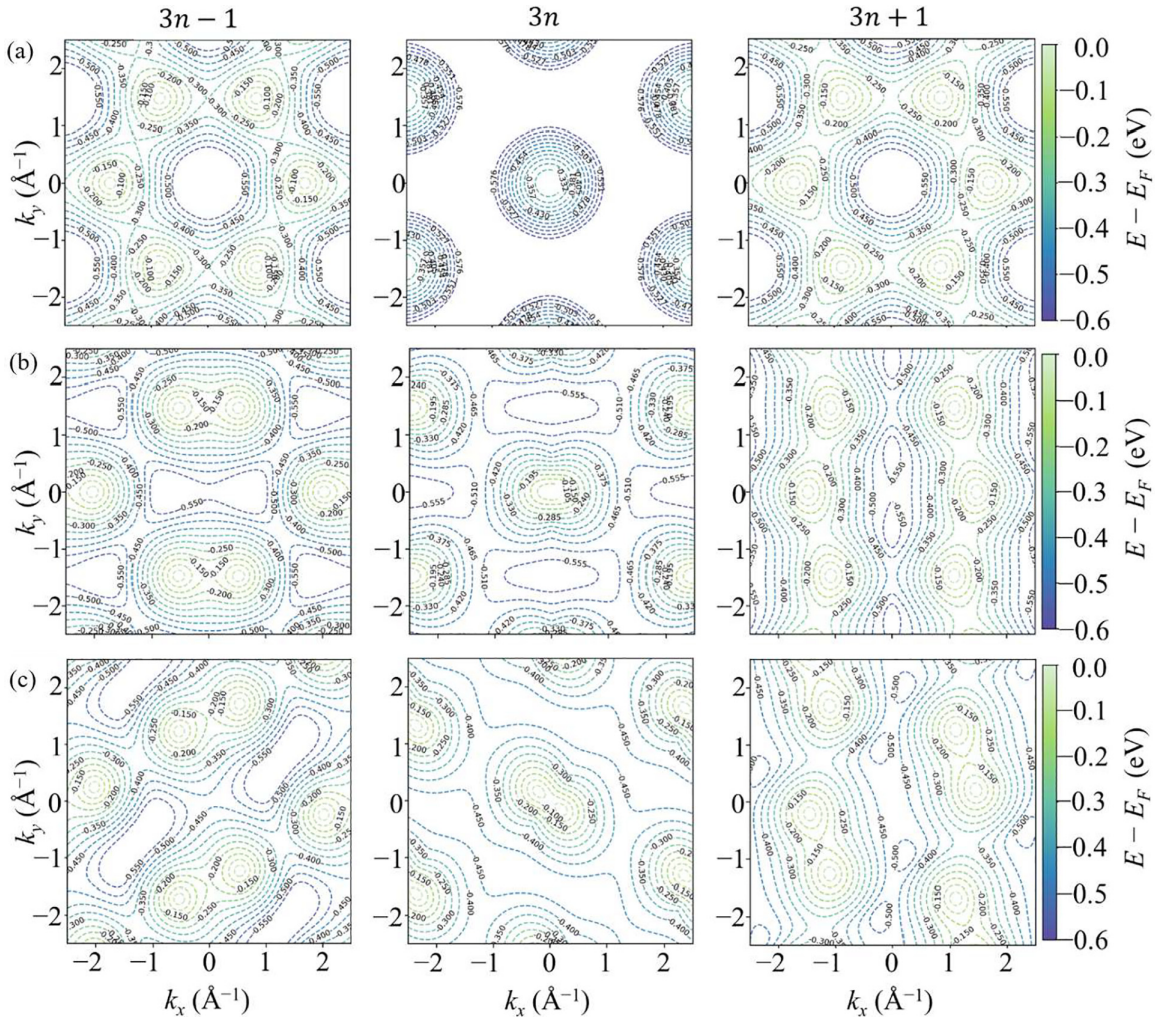


FIG. 7. Energy contour of the VBM in $3n-1$, $3n$, and $3n+1$ GSLs ($n=3$) with (a) $D_{3h(18C)}$, (b) $D_{2h(16C)}$, and (c) $C_{2(4C)}$.

118 meV, and $D_{2h(2C)}$ cannot open a band gap. In the 9×9 GSL, $D_{6h(6C)}$ gives a band gap 2.6 times larger than that of $D_{2h(10C)}$, making $D_{6h(6C)}$ the most efficient periodic vacancy motif for opening a band gap in the GSL. Therefore, the vacancy motifs can be ordered by increasing required defect concentration as $D_{6h(6C)} < C_{3h(12C)} < D_{3h(18C)} \ll D_{2h(10C)} < D_{2h(16C)}$. These results show that preserving C_3 symmetry is necessary to open a large band gap in $3n$ GSLs with periodic π vacancies. The C_2-type vacancies show band splitting of two degenerate bands at the VBM and CBM (ΔE_2), and the magnitude is comparable with the energy scale of the degenerate bands in C_3-type vacancies. This implies that K and K' are unequally split, lowering the magnitude of the band gap ΔE_1, as shown in Figs. 6(c) and 6(d).

C. The dispersion contour of the cones

The energy dispersion across the BZ can be represented by a Taylor expansion around the Dirac cone to second order and is given by [1,2,40,41]

$$E(\mathbf{q}) = \pm v_F|\mathbf{q}| - \left(\pm\frac{3t^2}{8}\sin(3\theta_q)\right)|\mathbf{q}|^2, \qquad (3)$$

where $\mathbf{k} = \mathbf{K} + \Delta\mathbf{q}$, $|\mathbf{q}| \ll |\mathbf{K}|$, and $\theta_q = \arctan(\frac{q_y}{q_x})$. The linear term $v_F|\mathbf{q}|$ gives a circular contour near the cones, while the second term introduces a threefold angular distortion (trigonal warping), making the energies further away from E_F dominated by the quadratic correction and the contour starts to warp [40,41]. The valley index in the angular term implies that the orientation of the trigonal warping at K and K' is reversed [42]. For small momentum near the Dirac cone, this distortion is weak, leading to circular contour. The shape of the energy dispersion can be visualized by plotting contours of the discrete $E(\mathbf{k})$. Figures 7(a)–7(c) show the dispersion contours of the VBM of the GSLs for $3n\pm 1$ and $3n$ sizes, with $n=3$. Figure 7(a) shows the dispersion contour of GSLs with $D_{3h(18C)}$ vacancy, where in $3n\pm 1$, the circular contours near the Dirac cones are clearly observed, while the trigonal shape appears at energies further away from Dirac points. Similarly, the dispersion remains circular near the VBM, indicating that it is isotropic near the energy level of the VBM. These patterns are observed in other GSLs with C_3 symmetry, as shown in Table II in the Supplemental Material [37], because C_3 enforces v_F to be equal in all directions and prevents anisotropy [43]. In contrast, C_2-type vacancies show elliptical contours both at energies close to and far from Dirac cones, indicating

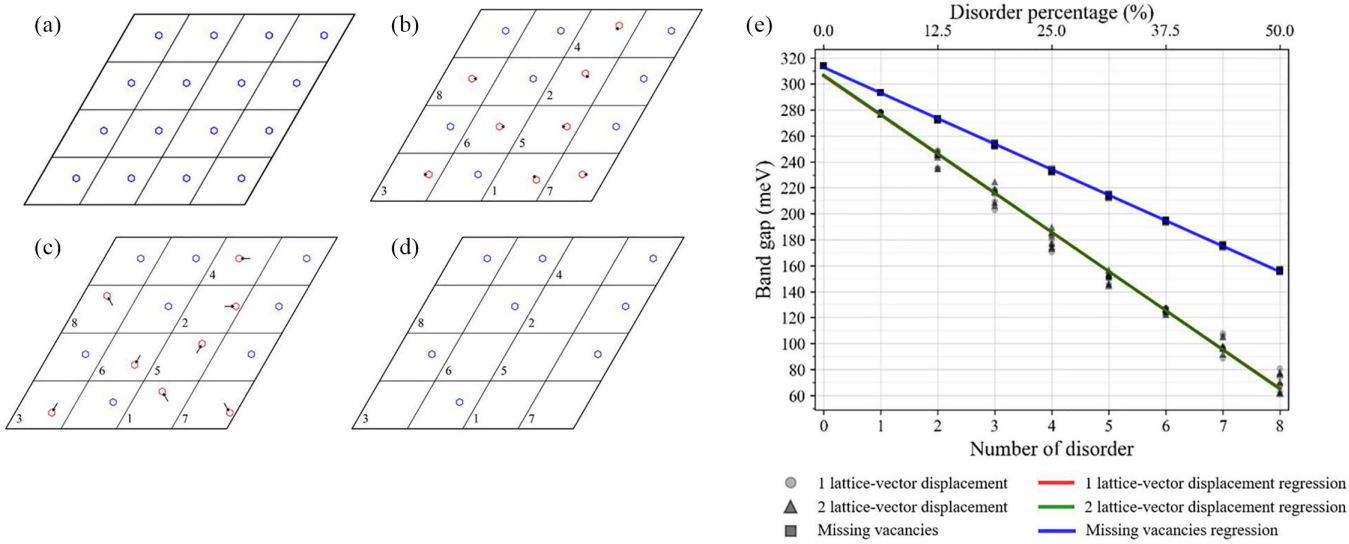


FIG. 8. (a) Ordered enlarged GSL containing 16 $D_{6h(6C)}$ vacancies, with each square representing one original GSL region containing one vacancy. (b) Representative displacement by one lattice vector from configuration 1. (c) Representative displacement by two lattice vectors from configuration 2. Red hexagons and arrows indicate the positions and directions of displaced vacancies. (d) Representative missing vacancy from configuration 3, with a blank box indicating a missing vacancy. (e) Band gap reduction as a function of the number of displaced or missing vacancies for different random configurations, along with the regression lines to show the band gap suppression trends.

anisotropic dispersion due to the breaking of C_3 symmetry. In the $3n$ GSLs that preserve $\sigma_d \perp \sigma_v$, such as $D_{2h(16C)}$ in Fig. 7(b) and Table II in the Supplemental Material [37], one elliptical contour at the VBM energy is observed, consistent with K and K' folding to Γ and allowing gap opening. However, in the $C_{2h(4C)}$ case, the mirror constraints are lifted and the cones can move away from Γ, appearing as two elliptical contours near Γ, as shown in Fig. 7(c). At higher energies, the anisotropic contribution becomes more pronounced, and there is no symmetry constraint enforcing trigonal warping. This means that the Fermi velocity in GSLs with C_2-type vacancies is no longer equal in all directions, suggesting potential for anisotropic transport applications.

D. Effect of periodicity-perturbing vacancy displacements and missing vacancies on the band gap

In experiments, achieving perfect long-range periodicity of π vacancies in graphene is challenging, and random positional disorder is expected in practical patterning approaches. In addition, vacancies may be missing during the fabrication process. To assess the robustness of the band gap opening against these imperfections, disorder simulations are done for the $D_{6h(6C)}$ vacancy in the 9×9 GSL superlattice. The perfect GSL has a defect concentration of 3.7% and a band gap of 314 meV. We construct an enlarged GSL from the $3n$ GSL with $n = 3$, by repeating it four times along each lattice direction, resulting in a GSL with 16 $D_{6h(6C)}$ vacancies, as shown in Fig. 8. We displace or remove up to 8 out of the 16 individual defects, as shown in Figs. 8(b) and 8(c) and Fig. 8(d), respectively, thereby perturbing the defect translational symmetry. Vacancy displacements were introduced by shifting the entire vacancy by one or two primitive lattice vectors of graphene from the perfect location, with the direction randomly selected from $\pm\mathbf{a}_1$, $\pm\mathbf{a}_2$, and $\pm(\mathbf{a}_2 - \mathbf{a}_1)$, as shown in Figs. 8(b) and 8(c), respectively. For each degree of disorder, five independent random configurations in terms of defect and its displacement direction were considered, as summarized in Table IV in the Supplemental Material [37]).

Figure 8(e) shows that the band gap decreases linearly as a function of the number of displaced or removed $D_{6h(6C)}$ vacancies. For displaced defects, the band gap decreases by 30 meV per defect and nearly closes at a 50% defect density. Missing vacancies also reduce the band gap linearly with concentration but by a smaller amount of 20 meV per defect (as shown in Fig. S3 and Table IV in the Supplemental Material [37]).

E. Symmetry-based guidelines for band gap opening in the GSL with periodic π vacancy

A general symmetry-based guideline for band gap opening in a GSL with periodic π vacancies can be formulated from our results, as shown in Fig. 9. At the TB level considered here, two base requirements ensuring that the π-network modulation can open the band gap in the GSLs are equal removal of sites of A and B sublattices, which avoids zero modes at E_F, and a uniform on-site energy on all remaining sites ($\varepsilon_i = \varepsilon_0$) to keep the sublattice symmetry. Under these conditions, the gap formation is controlled mainly by the symmetry constraints due to the π-vacancy modulation. The translational symmetry enforces GSL folding, and a band gap can be obtained effectively when the GSL size satisfies $3n$. The perturbation can occur when both K and K' valleys are folded to the TRIM point of Γ. In contrast, for $3n \pm 1$, the two valleys remain separated in momentum space, leaving the Dirac cone survive in the momentum space. Therefore, in practice, $3n$ GSL size is needed for π-vacancy gap engineering.

In these GSL sizes, the decisive factor becomes whether the vacancy pattern pins the folded cones at Γ and allows

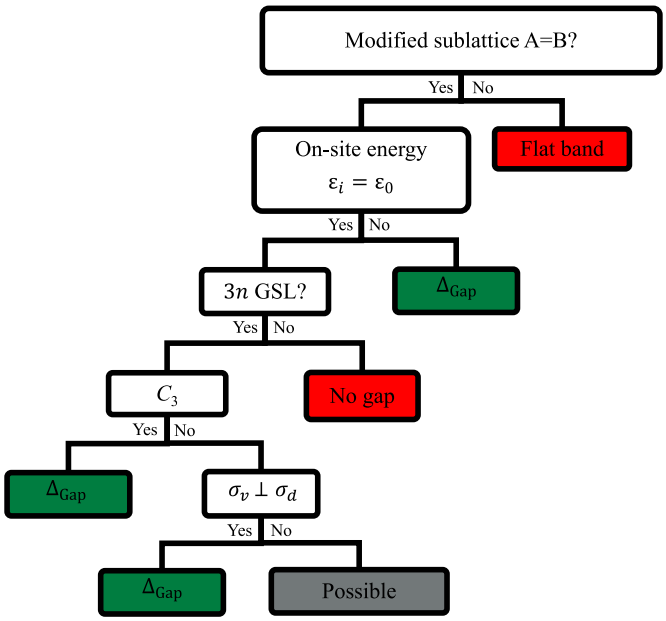


FIG. 9. An mBZ symmetry-based guideline to open the band gap in the GSL with periodic π vacancy.

the degeneracy to be lifted. Our results indicate two practical symmetry routes. The most robust route is to design a vacancy motif that preserves C_3 symmetry. In this case, threefold rotation constrains the cone positions to remain locked to high-symmetry points in the mBZ, enabling the gap opening at Γ in $3n$ GSLs and can be captured directly from high-symmetry sampling. Consistent with this, the C_3-type vacancies studied in this report generate larger band gaps at comparable defect concentrations than C_2-type vacancies. In particular, $D_{6h(6C)}$ is the most efficient motif in this study, achieving a large gap at a relatively low defect concentration, illustrating a benefit of preserving C_3. The second symmetry route is available for vacancy motifs without C_3. In these cases, a gap can still open in $3n$ GSLs if two perpendicular mirror planes $\sigma_d \perp \sigma_v$ are preserved in the mBZ. The remaining mirror planes restrict the Dirac cone shift along $k_\perp$; as a consequence, the cones are located at Γ in $3n$ GSLs, enabling gap opening. The perpendicular mirror planes $\sigma_d \perp \sigma_v$ are a sufficient condition but not necessary. However, in comparison with the C_3-preserving cases, the resulting gaps are smaller due to the nondegenerate bands. Hence, for experimental realizations where perfect periodicity is difficult to achieve, introducing a C_3-type vacancy is not only a practical route for band gap opening but also a route to a robust band gap against displacement. The π vacancies are models which can represent various defect types, such as hydrogenation leading to sp^3 functionalization [12,13,15] or BN substitution [5–7]. These changes maintain the graphene bonding framework but can result in local deformation, which in turn can quantitatively change the electronic structure but not the overall character of the band structure. In contrast, atomic vacancies give rise to strong relaxation effects with severe impact on the electronic structure of the GSL, as discussed elsewhere [44,45].

IV. CONCLUSIONS

In summary, we showed that periodic π vacancies in GSLs can induce band gap opening. Importantly, these results can be applied in broader defect engineering strategies, such as substitution, functionalization, or missing carbon sites. We found the following rules for opening a band gap in GSLs with periodic π vacancies: equal removal of sublattice A and B sites, with a uniform on-site energy at remaining sites, and a superlattice size of $3n$ is needed for folding K and K' to Γ. A feasible way to open the band gap is to preserve C_3 symmetry, which globally stabilizes the Dirac cone position at high-symmetry points, allowing K and K' to be pinned at Γ in $3n$ GSLs. Here, C_2-type vacancies can open a band gap if the perpendicular mirror planes $\sigma_v \perp \sigma_d$ are preserved in momentum space as a sufficient (but not necessary) condition. The C_3-type vacancies yield larger band gap, with $D_{6h(6C)}$ as the most efficient motif in terms of defect concentration, indicating the practical advantage of preserving C_3 symmetry. Vacancy disorder involving displacements by one or two primitive lattice vectors of graphene or missing $D_{6h(6C)}$ vacancies break the C_3 symmetry, lift the degeneracy, and reduce the gap toward the pristine graphene limit. For experimental realizations where perfect periodicity is difficult to achieve, introducing a C_3-type vacancy motif is therefore a practical route to large band gaps while maintaining robustness to displacement. We would like to point out that bottom-up precision synthesis approaches to functionalized graphene are a promising route to maintain the structural stability and a nearly linear dispersion of the electronic structure while opening a sizeable band gap of more than 500 meV in graphene, which is sufficient for stable electronics at room temperature.

ACKNOWLEDGMENTS

This work was funded by the Deutsche Forschungsgemeinschaft, through RTG 2861 “Planar Carbon Lattices” under Project No. 491865171 and through Project No. HE 3541–47-1. The authors gratefully acknowledge the computing time provided on the high-performance computer at the ZIH.

DATA AVAILABILITY

The data that support the findings of this article are given in the manuscript or in the Supplemental Material [37].

[1] P. R. Wallace, The band theory of graphite, Phys. Rev. **71**, 622 (1947).

[2] A. H. Castro Neto, F. Guinea, N. M. R. Peres, K. S. Novoselov, and A. K. Geim, The electronic properties of graphene, Rev. Mod. Phys. **81**, 109 (2009).

[3] K. S. Novoselov, A. K. Geim, S. V. Morozov, D. Jiang, M. I. Katsnelson, I. V. Grigorieva, S. V. Dubonos, and A. A. Firsov, Two-dimensional gas of massless Dirac fermions in graphene, Nature (London) **438**, 197 (2005).

[4] K. S. Novoselov, A. K. Geim, S. V. Morozov, D. Jiang, Y. Zhang, S. V. Dubonos, I. V. Grigorieva, and A. A. Firsov, Electric field effect in atomically thin carbon films, Science **306**, 666 (2004).

[5] F. Joucken, Y. Tison, J. Lagoute, J. Dumont, D. Cabosart, B. Zheng, V. Repain, C. Chacon, Y. Girard, A. R. Botello-Méndez, *et al.*, Localized state and charge transfer in nitrogen-doped graphene, Phys. Rev. B **85**, 161408(R) (2012).

[6] T. G. Pedersen and J. G. Pedersen, Self-consistent tight-binding model of B and N doping in graphene, Phys. Rev. B **87**, 155433 (2013).

[7] J. Gebhardt, R. J. Koch, W. Zhao, O. Höfert, K. Gotterbarm, S. Mammadov, C. Papp, A. Görling, H.-P. Steinrück, and T. Seyller, Growth and electronic structure of boron-doped graphene, Phys. Rev. B **87**, 155437 (2013).

[8] A. Lherbier, S. M.-M. Dubois, X. Declerck, Y.-M. Niquet, S. Roche, and J.-C. Charlier, Transport properties of graphene containing structural defects, Phys. Rev. B **86**, 075402 (2012).

[9] T. G. Pedersen, C. Flindt, J. Pedersen, N. A. Mortensen, A.-P. Jauho, and K. Pedersen, Graphene antidot lattices: Designed defects and spin qubits, Phys. Rev. Lett. **100**, 136804 (2008).

[10] F. Ouyang, S. Peng, Z. Liu, and Z. Liu, Bandgap opening in graphene antidot lattices: The missing half, ACS Nano **5**, 4023 (2011).

[11] S. Lebègue, M. Klintenberg, O. Eriksson, and M. I. Katsnelson, Accurate electronic band gap of pure and functionalized graphane from GW calculations, Phys. Rev. B **79**, 245117 (2009).

[12] R. Balog, B. Jørgensen, L. Nilsson, M. Andersen, E. Rienks, M. Bianchi, M. Fanetti, E. Laegsgaard, A. Baraldi, S. Lizzit, *et al.*, Bandgap opening in graphene induced by patterned hydrogen adsorption, Nat. Mater. **9**, 315 (2010).

[13] S. Ryu, M. Y. Han, J. Maultzsch, T. F. Heinz, P. Kim, M. L. Steigerwald, and L. E. Brus, Reversible basal plane hydrogenation of graphene, Nano Lett. **8**, 4597 (2008).

[14] C. - Y. Hou, C. Chamon, and C. Mudry, Electron fractionalization in two-dimensional graphenelike structures, Phys. Rev. Lett. **98**, 186809 (2007).

[15] J. Tuček, K. Holá, A. B. Bourlinos, P. Błoński, A. Bakandritsos, J. Ugolotti, M. Dubecký, F. Karlický, V. Ranc, K. Čépe, *et al.*, Room temperature organic magnets derived from sp^3 functionalized graphene, Nat. Commun. **8**, 14525 (2017).

[16] E. A. Kolesov, M. S. Tivanov, O. V. Korolik, V. A. Skuratov, O. O. Kapitanova, and G. N. Panin, Ion irradiation of supported graphene: Defect formation and atmospheric doping, Mater. Sci. Eng. B **284**, 115918 (2022).

[17] W. Li, X. Wang, X. Zhang, S. Zhao, H. Duan, and J. Xue, Mechanism of the defect formation in supported graphene by energetic heavy ion irradiation: The substrate effect, Sci. Rep. **5**, 9935 (2015).

[18] A. J. M. Giesbers, E. C. Peters, M. Burghard, and K. Kern, Charge transport gap in graphene antidot lattices, Phys. Rev. B **86**, 045445 (2012).

[19] J. Bai, X. Zhong, S. Jiang, Y. Huang, and X. Duan, Graphene nanomesh, Nat. Nanotechnol. **5**, 190 (2010).

[20] C. Moreno, M. Vilas-Varela, B. Kretz, A. Garcia-Lekue, M. V. Costache, M. Paradinas, M. Panighel, G. Ceballos, S. O. Valenzuela, D. Peña, *et al.*, Bottom-up synthesis of multifunctional nanoporous graphene, Science **360**, 199 (2018).

[21] M. Bieri, M. Treier, J. Cai, K. Aït-Mansour, P. Ruffieux, O. Gröning, P. Gröning, M. Kastler, R. Rieger, X. Feng, *et al.*, Porous graphenes: Two-dimensional polymer synthesis with atomic precision, Chem. Commun. **45**, 6919 (2009).

[22] T. Qin, T. Wang, and J. Zhu, Recent progress in on-surface synthesis of nanoporous graphene materials, Commun. Chem. **7**, 154 (2024).

[23] D. Wang, X. Lu, M. Y. Arramel, J. Wu, and A. T. S. Wee, On-surface synthesis of variable bandgap nanoporous graphene, Small **17**, e2102246 (2021).

[24] M. Wang, L. Fu, L. Gan, C. Zhang, M. Rümmeli, A. Bachmatiuk, K. Huang, Y. Fang, and Z. Liu, CVD growth of large area smooth-edged graphene nanomesh by nanosphere lithography, Sci. Rep. **3**, 1238 (2013).

[25] L. Esaki and R. Tsu, Superlattice and negative differential conductivity in semiconductors, IBM J. Res. Dev. **14**, 61 (1970).

[26] C.-H. Park, L. Yang, Y.-W. Son, M. L. Cohen, and S. G. Louie, Anisotropic behaviours of massless Dirac fermions in graphene under periodic potentials, Nat. Phys. **4**, 213 (2008).

[27] W. Oswald and Z. Wu, Energy gaps in graphene nanomeshes, Phys. Rev. B **85**, 115431 (2012).

[28] M. Mieda and S. Okada, Energetics and electronic structures of polymeric all-benzene hollow-cages and planar networks, Jpn. J. Appl. Phys. **58**, 015002 (2019).

[29] V. M. Pereira, J. M. B. Lopes dos Santos, and A. H. Castro Neto, Modeling disorder in graphene, Phys. Rev. B **77**, 115109 (2008).

[30] T.-T. Jia, M.-M. Zheng, X.-Y. Fan, Y. Su, S.-J. Li, H.-Y. Liu, G. Chen, and Y. Kawazoe, Dirac cone move and bandgap on/off switching of graphene superlattice, Sci. Rep. **6**, 18869 (2016).

[31] T. Ochiai and M. Onoda, Photonic analog of graphene model and its extension: Dirac cone, symmetry, and edge states, Phys. Rev. B **80**, 155103 (2009).

[32] J. Ding, Z. Qiao, W. Feng, Y. Yao, and Q. Niu, Engineering quantum anomalous/valley Hall states in graphene via metal-atom adsorption: An *ab-initio* study, Phys. Rev. B **84**, 195444 (2011).

[33] V. V. Cheianov, V. I. Fal'ko, O. Syljuåsen, and B. L. Altshuler, Hidden Kekulé ordering of adatoms on graphene, Solid State Commun. **149**, 1499 (2009).

[34] S. L. Xiu, L. Gong, V. Wang, Y. Y. Liang, G. Chen, and Y. Kawazoe, Degenerate perturbation in band-gap opening of graphene superlattice, J. Phys. Chem. C **118**, 8174 (2014).

[35] S. Coh, D. Vanderbilt, and T. Cole, Python Tight Binding (PythTB), Zenodo (2025) http://10.5281/zenodo.12721316.

[36] E. H. Lieb, Two theorems on the Hubbard model, Phys. Rev. Lett. **62**, 1201 (1989).

[37] See Supplemental Material at http://link.aps.org/supplemental/10.1103/nbm9-xhj9 for additional band structures, symmetry analyses, and energy contours of other vacancy motifs, together with the disorder configurations and corresponding regression analyses for displaced and missing vacancies.

[38] J. J. Palacios, J. Fernández-Rossier, and L. Brey, Vacancy-induced magnetism in graphene and graphene ribbons, Phys. Rev. B **77**, 195428 (2008).

[39] M. M. Ugeda, I. Brihuega, F. Guinea, and J. M. Gómez-Rodríguez, Missing atom as a source of carbon magnetism, Phys. Rev. Lett. **104**, 096804 (2010).

[40] T. Ando, Theory of electronic states and transport in carbon nanotubes, J. Phys. Soc. Jpn. **74**, 777 (2005).

[41] M. S. Dresselhaus and G. Dresselhaus, Intercalation compounds of graphite, Adv. Phys. **51**, 1 (2002).

[42] E. McCann, Electronic Properties of Monolayer and Bilayer Graphene, in *Graphene Nanoelectronics: Metrology, Synthesis, Properties and Applications*, edited by H. Raza (Springer, Berlin, 2012), pp. 237–276.

[43] I. F. Herbut, Explanation for the isotropy of the Dirac cone in graphene, Phys. Rev. B **79**, 193405 (2009).

[44] A. A. El-Barbary, R. H. Telling, C. P. Ewels, M. I. Heggie, and P. R. Briddon, Structure and energetics of the vacancy in graphite, Phys. Rev. B **68**, 144107 (2003).

[45] G.-D. Lee, C. Z. Wang, E. Yoon, N.-M. Hwang, D.-Y. Kim, and K. M. Ho, Diffusion, coalescence, and reconstruction of vacancy defects in graphene layers, Phys. Rev. Lett. **95**, 205501 (2005).